International Conference on Space Optics—ICSO 2022

Dubrovnik, Croatia

3–7 October 2022

Edited by Kyriaki Minoglou, Nikos Karafolas, and Bruno Cugny,

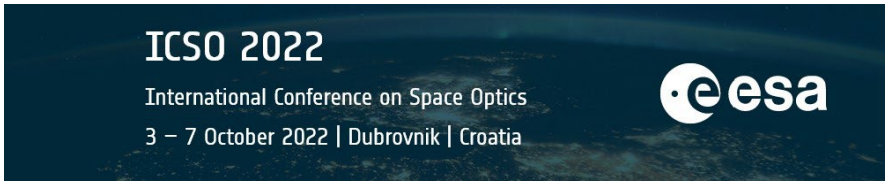

Lifetime and radiation tests results on Hi-QE Blue MCP-PMTs for spaceborne UV LIDAR receivers

International Conference on Space Optics — ICSO 2022, edited by Kyriaki Minoglou, Nikos Karafolas, Bruno Cugny, Proc. of SPIE Vol. 12777, 127771J · © 2023 ESA and CNES · 0277-786X · doi: 10.1117/12.2689293

Lifetime and Radiation tests results on Hi-QE Blue MCP-PMTs for spaceborne UV LIDAR receivers

Alex MATERNE*[a], Olivier GILARD[a], Marine RUFFENACH[a], Frédéric BOURCIER[a]
Olivier SAINT PE[b], Xavier DURAND[b], Dmitry ORLOV[c], Emilie KERNEN[c],
René GLAZENBORG[c], Guillaume THIN[d]
[a]CNES, Centre National d'Etudes Spatiales, 18 avenue Edouard BELIN, 31401 Toulouse Cedex France; [b]Airbus Defence & Space, 31 rue des cosmonautes 31402 Toulouse Cedex 4 France;
[c]Photonis, Dwazziewegen 2, 9301ZR Roden, The Netherlands;
[d]Intraspec Technologies, 20 Av. Didier Daurat, 31400 Toulouse France

ABSTRACT

Thanks to a large set of available photocathodes with first in class QE, high gain, high collection efficiency, high dynamic range while keeping low dark count rate and single photon resolution capability with excellent timing, MCP-PMTs have emerged as candidates for LIDAR receivers.
We present results of Ageing tests and Radiation tests carried out with Photonis and Airbus Defence & Space on High QE, and High linearity MCP-PMT for UV LIDAR receivers.
Ageing of the photocathode is usually due to electron-induced ion feedback and molecule desorption from the MCP and anode, causing degradation of the photocathode layer leading to a progressive loss of QE related to the quantity of electron charges generated along lifetime.
Expected Coulomb charges generated along a typical and worst-case mission were estimated from the atmosphere profiles. Thanks to a design change of the MCP-PMT and the implementation of Long-Lifetime MCP technology, ageing of the photocathode was drastically reduced. The new design showed no Quantum Efficiency nor Collection Efficiency degradation up to 20 C.
Proton radiation tests were performed to evaluate false signal generated, end-of-life impact on performance, loss of transmission depending on the photocathode glass substrate as well as cathodoluminescence and photoluminescence at the photocathode.
Quantum Efficiency, Collection Efficiency, PHD shape, Gain, and Linearity were found to be unchanged for fluences of $5x10^{11}$ p+/cm² with 60 MeV protons. Only small increase of DCR for about 120 cps/cm² was recorded about 8 weeks after the radiation.

Keywords: MCP-PMT, LIDAR, radiation, photocathode, lifetime

1. INTRODUCTION

Detectors for receivers of LIDARs for Earth Atmosphere sounding of Clouds and Aerosols must achieve several basic requirements:

- They must be able to provide an optical bandwidth sensitivity that extends over the three Nd:YAG wavelengths 355 nm, 532 nm, 1064 nm,
- They must present good linear behaviour over a dynamic range that starts from photon fluxes as low as 10^5 ph/s and peaks at about 10^{10} ph/s, and even 10^{12} ph/s including ground echo, with laser repetition rate around a hundred of Hertz and ground echo duration of several tens of nanoseconds
- They must feature a high speed response to follow the trend toward finer vertical resolutions down to 1 m for bathymetry.

The first LIDAR echo profile of the Earth atmosphere was acquired by the LITE LIDAR[1] on-board of Discovery in 1994. Then several space LIDAR missions for Cloud and Aerosols sounding were launched (ICEsat1 2003[2], CALIOP 2006[3]). The detectors selected for these first missions were photomultiplier tubes (LITE 355 and 532 nm, CALIOP 532 nm) or Silicon Avalanche Photodiodes (LITE 1064 nm, ICEsat1/GLAS 532 nm, CALIOP 1064 nm).

*alex.materne@cnes.fr; phone 33561281544 ;

Photo-multiplier tubes are still used but suffer from poor quantum efficiency, and generate operating constraints in space environment.
Silicon APD present larger manufacturability, easier operating conditions, but reduced gain and high excess noise factor.

ALADIN LIDAR on ADM Aeolus[4] mission launched in 2018 for wind profiles measurements features an accumulation CCD manufactured by e2v UK.
Accumulation CCDs (ACCD) show good signal to noise performance thanks to an analogue accumulation of the return signal. But they request small sampling frequency and show reduced optical bandwidth. Moreover, the accumulation CCD suffer from transfer inefficiency on very weak signals and have shown in-flight occurrence of hot pixels issues[5].
Progress in technologies and extended requirements in dynamic range, temporal resolution, spectral band, or bathymetry capability opened the way to new candidates such as InGaAs APD, Si-PM[6] and MCP-PMT[7].
Trend to better vertical resolution needs fast temporal response.

InGaAs APDs allow to detect wavelengths up to 1.7 µm, as for the MERLIN[8] mission aimed at methane sounding in the Earth atmosphere. They present however some limitations due to low gain and high excess noise factor.

Silicon Photo-Multipliers (Si-PM) are very promising, thanks to high gains and small excess noise factors as well as good industrial feasibility. They lack at covering a large optical bandwidth, and reveal significant Dark count rate degradation due to radiation environment in Space[9]. Thanks to significant efforts to reduce their radiation sensitivity, they should overcome this drawback in a near future.

Micro Channel Plate Photomultiplier Tube (MCP-PMT) emerge as good candidates for LIDAR missions due to a large set of photocathodes, with low dark count, high gain, high dynamic range and excellent temporal resolution.
MCP-PMT use a photocathode to convert incoming photons in electrons, then Micro Channel Plates under high electrical field are used as electron multiplier stage and one (in our case) or several anodes are collecting pulses.
We started our first characterization of a MCP-PMT in 2018, in the frame of a CNES and Airbus Defence & Space R&D joined activity. Photonis was selected as detector provider for its expertise and willing to progress in space applications. First steps included performance assessment and construction analysis. On the basis of the construction analysis, we kept on with an evaluation program which we planned to focus on a mechanical file with shock and vibrations, then characterization of the ageing process at the photocathode, proton radiation impacts and cathodoluminescence of the window.

This paper presents the main results of our test program carried out with Photonis and Airbus Defence & Space on a Hi QE, Hi linearity MCP-PMT.

2. THE UV CHANNEL FOR MESCAL

This work was initially started to consolidate the French contribution to the MESCAL (Monitoring the Evolving State of Clouds and Aerosols Layers) LIDAR program managed by NASA in the frame of the A-CCP (Aerosols and Cloud-Convection Precipitation) study. The French Team promoted the 355 nm channel to ensure data correlation between CALIOP (for green and NIR) and EARTHCARE (for UV)[10] as well as better speciation of aerosol types.
MESCAL is a type of up-graded follow-on of CALIOP, with the HSRL (High Spectral Resolution LIDAR) capability that allows to discriminate aerosols and molecules thanks to multi-wavelength measurements[11]. MESCAL targets a 10 meters vertical resolution for aerosols and clouds and 1 meter resolution for bathymetry.

The 355 nm channel was finally abandoned in 2021, with no correlation with the results obtained so far on the Photonis MCP-PMT detectors which demonstrated good performance after the evaluation tests we present hereafter.
So the requirements and environment constraints were, as much as possible, based on MESCAL expected orbits and photon fluxes at the receiver input, schematically shown on Figure 1.

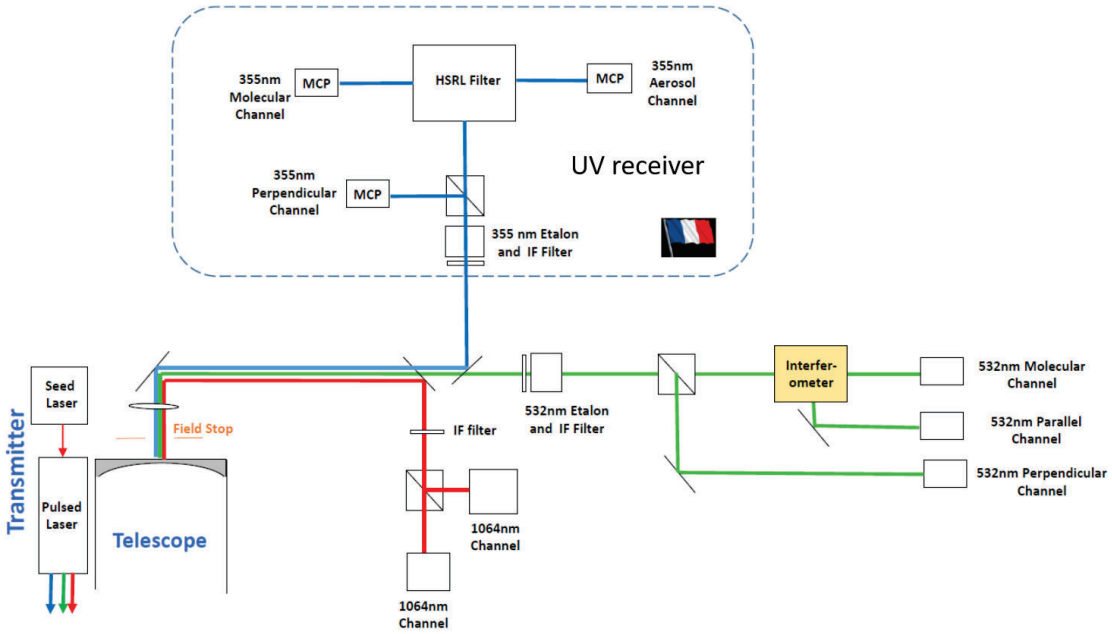

Figure 1. Initial joined CNES-NASA LaRC architecture for MESCAL. The UV receiver was the French contribution. It was abandoned in 2021.

Three cases of illumination are illustrated below in Figures 2. The figures show three laser echo profiles ("useful flux" in photon/s along Y-axis) corresponding to the three different reception channels to be implemented on the UV receiver (these profiles may overlap over certain altitudes). Note that fluxes below 10^5 photon/s were considered not relevant for the mission.

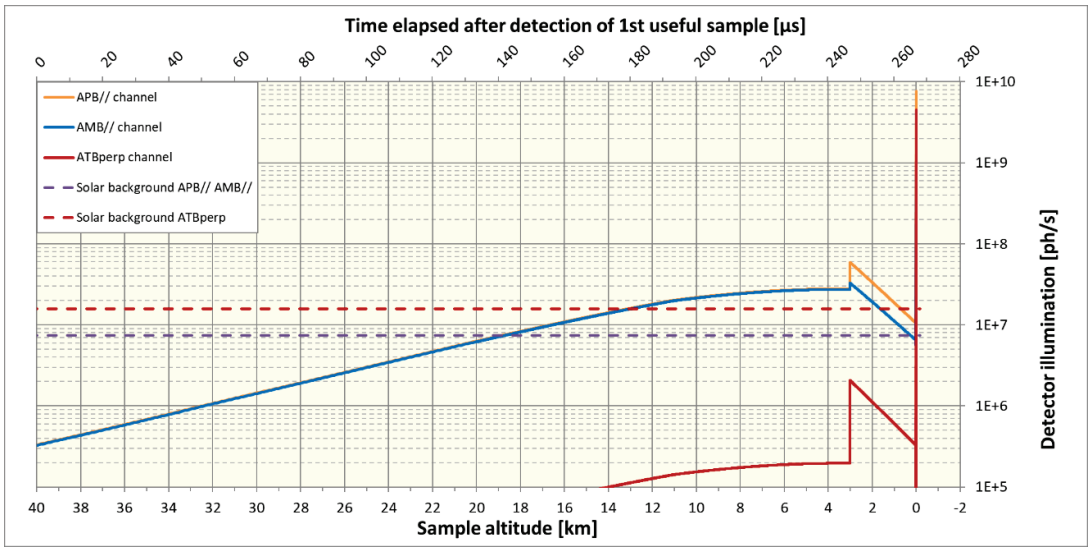

Figure 2(a). LIDAR profiles for 355 nm wavelength, at 450 km altitude. Typical case for cloud free atmosphere with aerosols over vegetation. Two equivalent X-axis are provided, allowing the profiles to be read either versus altitude with respect to ground level (in kilometers), or time elapsed after reception of 40km-altitude echo (in microseconds).

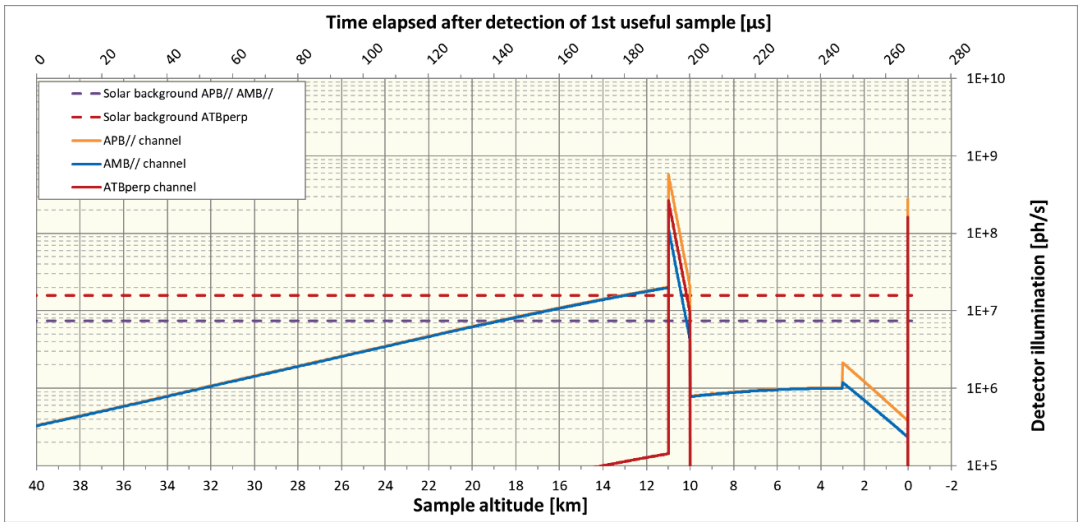

Figure 2(b). LIDAR profiles for 355 nm wavelength, at 450 km altitude. Typical case for atmosphere with aerosols and clouds.

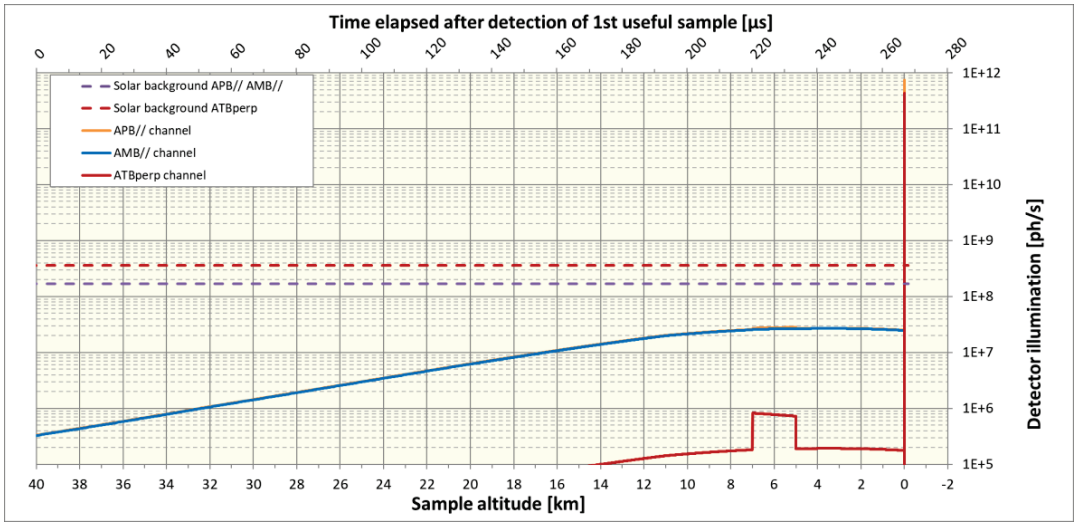

Figure 2(c). LIDAR profiles for 355 nm wavelength, at 450 km altitude. Worst case for atmosphere with presence of faint clouds in clean atmosphere over snow.

In addition to the laser echo, solar background also contributes to detector illumination (except during night time). Levels displayed in the figure are the maximum levels expected during daytime at detector-level.

3. THE FAST TIMING MCP PMT

The Multi Channel Plate Photo Multiplier Tube (MCP-PMT) selected for the UV channel receiver is a Gateable Fast Timing MCP-PMT with 18mm open area (FT18-MCP-PMT) designed and manufactured by Photonis, with a low noise Hi-QE Blue photocathode on Quartz input window and single anode, with a typical QE spectrum shown on Figure 3.

Its main performances and capability to handle photon counting as well as large signals due to ground echo as required for Space LIDAR for atmosphere sounding applications has been previously presented by Photonis[12,13].

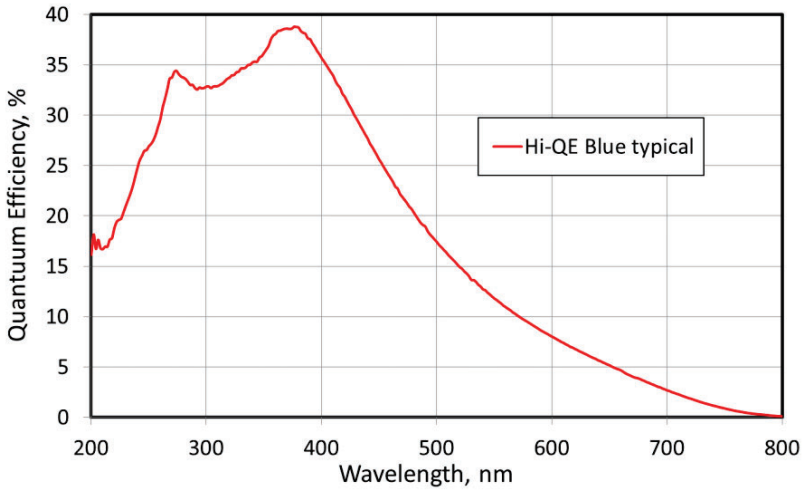

Figure 3. Quantum Efficiency (QE) of the Hi-QE blue photocathode of the Photonis FT18-MCP-PMT.

Table 1 gives the main performance of the Hi QE, Hi- linearity model of MCP-PMT.

Table 1. Specification of model series FT-18 MCP-PMT @ 25°C and nominal operation voltage (- 2300 V).

	Min	Typ	Max	Unit
Input useful diameter	17.5	18.0		
QE of photocathode @355 nm	27	30		%
MCP collection efficiency (CE)	90	95		%
Gain	$9\ 10^4$	$2\ 10^5$	$4\ 10^5$	
Linearity @75%	300	500		MHz
Photocathode dark count rate		70	100	cps
Time response rise time FWHM		 180 400	 250 500	 ps ps

4. RESULTS

4.1. Vibration and Shock

The mechanical tests sequence consisted in:

- Initial resonance survey test
- Vibration
- Shock
- Final resonance survey test to check no occurrence of change in the spectrum.

The sequence was successfully implemented on two Hi QE blue devices with the test conditions given in Table 2. All performances were tested before and after the mechanical sequences showing no degradation.

Table 2. Mechanical tests conditions.

VIBRATION SPECIFICATIONS
Typical specifications
Stiffness > 200 Hz intermediate levels
Random - Random: 0.25 g²/Hz in the range [100 Hz, 700 Hz] 0.075 to 0.1 g2/Hz
Slope 3dB octave/band before 100Hz and -6dB/oct after 700Hz, 120s, 3 axes about 14 gRMS
QS - Quasi-static: sweep 35g from 40Hz to 150 Hz, 2oct/min, 3 axes 17g
Shock shock level ½ sine 100g, 0.5 ms 3 axis, 2 directions + and – per axis 50g 0.5ms
Conservative specifications
Stiffness > 200 Hz
Random - Random: 0.5 g²/Hz in the range [100 Hz, 700 Hz]
Slope 3dB octave/band before 100Hz and -6dB/oct after 700Hz, 120s, 3 axes about 20 gRMS
QS - Quasi-static: sweep 50g from 40Hz to 150 Hz, 2oct/min, 3 axes
SHOCK SPECIFICATIONS
Shock 100Hz : 20g (all axis)
1000Hz : 1000g (all axis)
10000Hz : 1000g (all axis)

4.2. Lifetime tests

Reduction of the photocathode Quantum Efficiency (QE) during operating life is a known issue[13].
Figure 4 shows QE evolution with charge extracted obtained on a commercial S20 Hi-QE Blue MCP-PMT at nominal MCP gain of 10^5. The photocathode surface (18 mm diameter) was homogeneously illuminated with a 400 nm LED source.

Ageing of the photocathode is usually due to electron-induced ion feedback and molecule desorption from the MCP and anode, causing degradation of the photocathode layer leading to a progressive loss of QE related to the quantity of electron charges generated along lifetime.

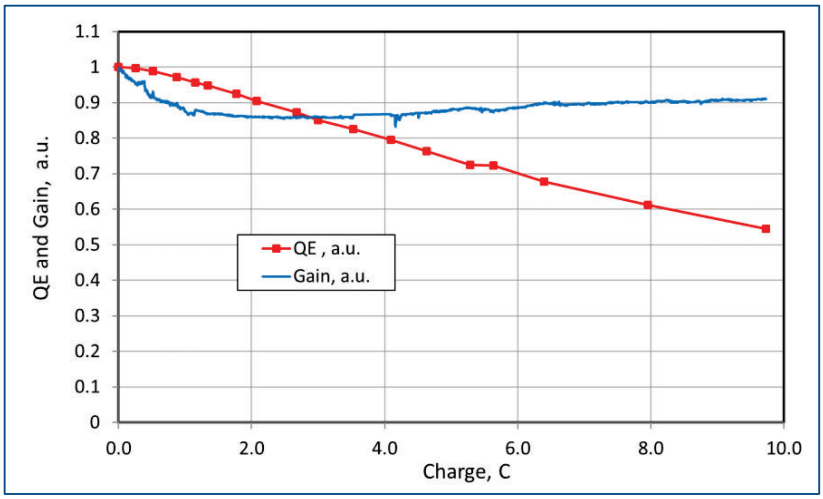

Figure 4. Relative change of quantum efficiency at 400 nm and gain vs total charge extracted from the anode, with extrapolated lifetime of about 4 C and 10 C for 20% and 50% QE drop, respectively[13].

Expected Coulomb charges generated along a typical and worst-case mission, taking into account a necessary gating of the detector due to the large solar background during day measurements, were estimated from the atmosphere profiles to be about 6C, corresponding to 33% of QE drop (Fig.4).
Gating consists in a synchronized switching of the high voltage supplied between photocathode and micro channel plates, in order to limit the operating time window of the MCP-PMT during a 400 µs time interval of the laser period of 14 ms, when a useful signal is expected.
This gating strategy reduces the background-induced load on lifetime by the reverse of the duty ratio.

In order to maintain the initial QE over the mission duration of ten years, and/or allow higher operating gain, a Long Lifetime MCP design was tested.

The new design – that mainly consists in preventing the ion feedback at the photocathode was tested with results presented in Figure 5, showing no QE degradation at all measured wavelengths up to 19 C. Other performances remained as well unchanged. The test included 4.7 10^{10} gating cycles that were added to the test conditions within the last generated charge of 1.4 Coulombs.

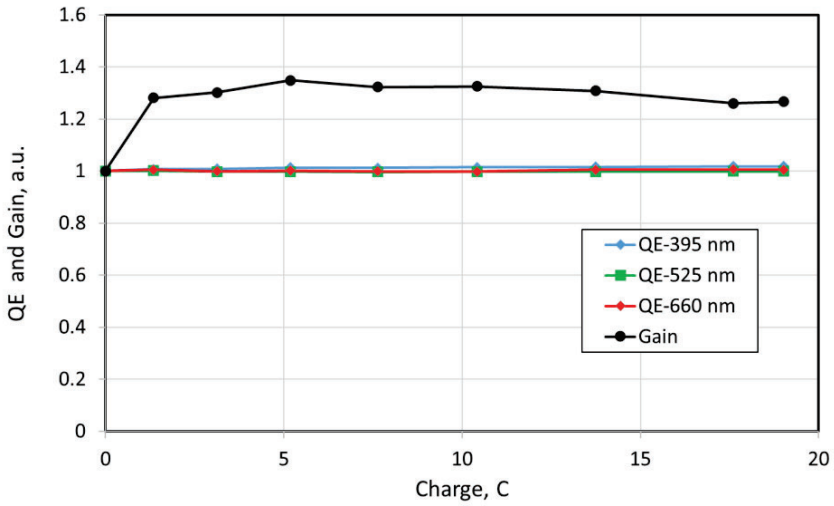

Figure 5. Relative change of quantum efficiency at 3 wavelengths and gain vs total charge extracted from the anode of the Long Lifetime FT18-MCP-PMT.

4.3. Protons radiation

Impact of space radiations must be characterized first because radiations may change the basic performance of the detectors, and second because radiations may induce false events that corrupt the total photon counting.

Protons radiation was deliberately performed in conditions that will cover multiple LEO missions.
The total fluence depends on many parameters, including instrument shielding geometry, orbital parameters like altitude and inclination, and others.
The total in-flight proton fluence was estimated to be 1.8 10^{11} p/cm2 for 60 MeV protons, assuming typical instrumental shielding equivalent to 4 mm aluminum, and a worst case 800 km orbit. This TNID would correspond to a total ionizing dose (TID) of 20 krad (Si) accumulated in the full mission lifetime of 10 years.
The proton radiation campaign was implemented by the Photonis team at KVI facility, in Groningen (The Netherlands).

Protons radiation of window substrates

A first phase consisted in measuring loss of transmission and photoluminescence (under excitation with 400 nm laser) in Photonis labs and then cathodoluminescence in CNES labs before and after radiation of several photocathode substrates: quartz substrates (FT18-MCP-PMT has a quartz based photocathode) and Borosilicate glass for comparison.

The Borosilicate glass was found to be impacted in the UV range with a 60 % loss of transmission at 350 nm after 5 10^{11} p/cm².

The photoluminescence measurements after the radiation for the glass substrate samples radiated with highest dose of 5 10^{11} p/cm² are shown on the Figure 6 (bottom) together with reference sample #21 (which did not undergo radiation). For quartz based substrates no change was found with very weak photoluminescence signal above 440 nm, that is in correlation with transmission measurements where no radiation-induced loss of transmission was observed.

On the other hand, a strong increase of photoluminescence signal (almost by 2 orders of magnitude above 850 nm) was found for the Borosilicate glass substrate. From transmission measurements, we know that after radiation this sample absorbs almost 50% of 405 nm light. From strong increase of photoluminescence in visible and infra-red part (and with photoluminescence shape to be about the same as before radiation) we can conclude that some part of absorbed laser photons recombine through the same radiative centers which were present in the glass before radiation. No additional strong photoluminescence peaks were observed in the photoluminescence spectrum.

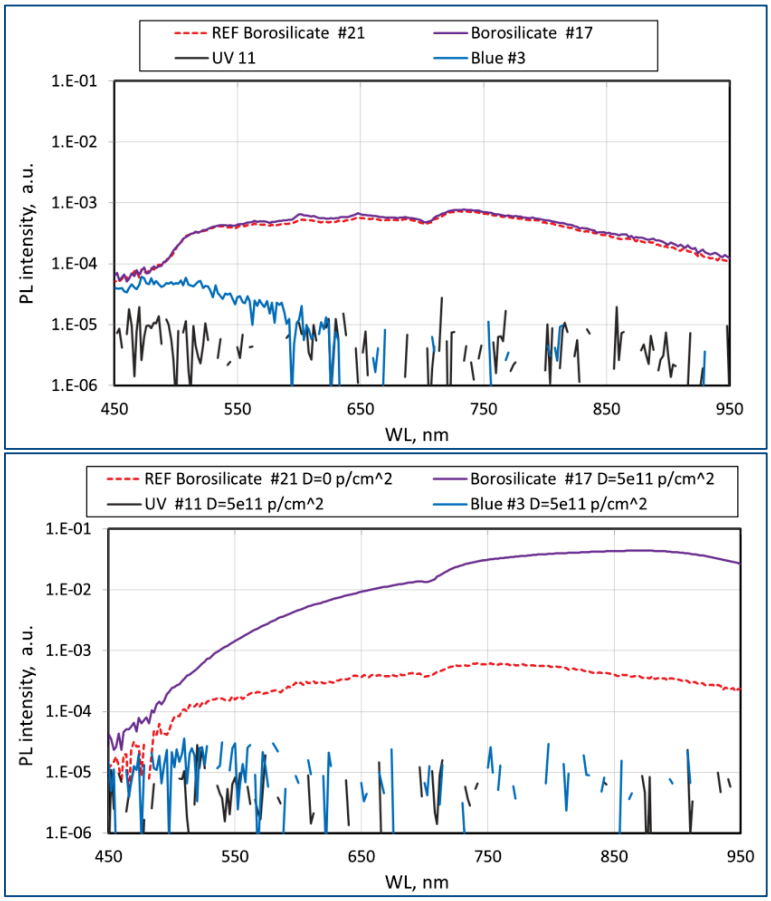

Figure 6. Photoluminescence- under 400 nm laser- measurements before (upper figure) and after the radiation (lower figure) of the glass substrate samples: non-irradiated ref sample Borosilicate (red dots) ; Borosilicate (purple) ; Hi QE UV quartz (black line) and Hi QE blue quartz (blue line).

Measurements of the cathodoluminescence of these glasses have then been performed at CNES to estimate the risk of parasitic light emission. The cathodoluminescence has been obtained using the electron beam of a scanning electron microscope.

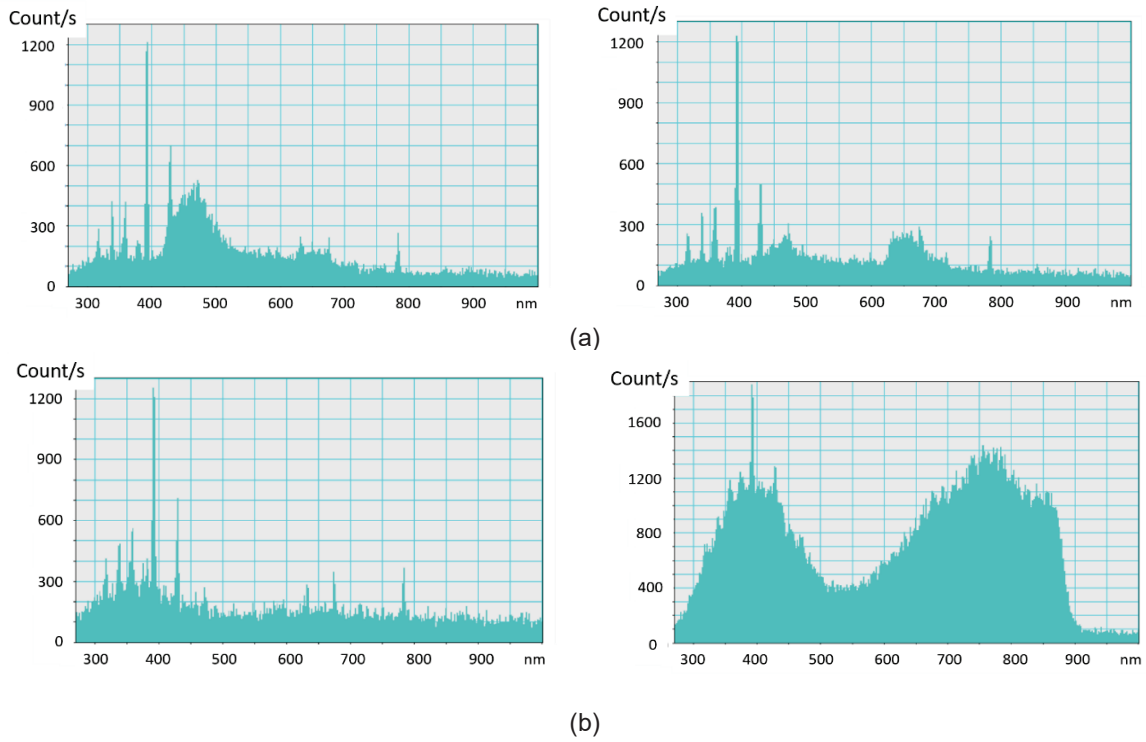

Figure 7. Cathodoluminescence spectra of quartz (a) and borosilicate glass (b) before (left) and after (right) 5 10^{11} p+ (60 MeV)/cm² exposure. The electron beam energy to activate the cathodoluminescence was set to 15 keV.

The cathodoluminescence is fairly weak for quartz samples before and after radiation but the borosilicate glass shows a significant increase of the cathodoluminescence after irradiations, correlating with the photoluminescence results.

Protons radiation of MCP PMT

Radiation with 60 MeV protons up to a fluence of 5 10^{11} p+/cm² was carried out at a flux of 1.45 10^{8} p/s/cm² on two high-linearity Hi-CE Hi-QE blue MCP-PMT.

At this high flux it was observed that single proton generates about 10 effective electrons with about 70 % originated from photocathode (~7 él/p+ from photocathode and ~3 él/p+ from MCP).

It is thought that the photocathode contribution is mainly due to the energy loss within the glass window (may be related to scintillation) and not because of a direct interaction between the protons and the photocathode layer.

Main performances were measured 7-8 weeks after radiations. QE and CE were found unchanged.

No recognizable change was found in the gain (figure 8) and PHD shape.

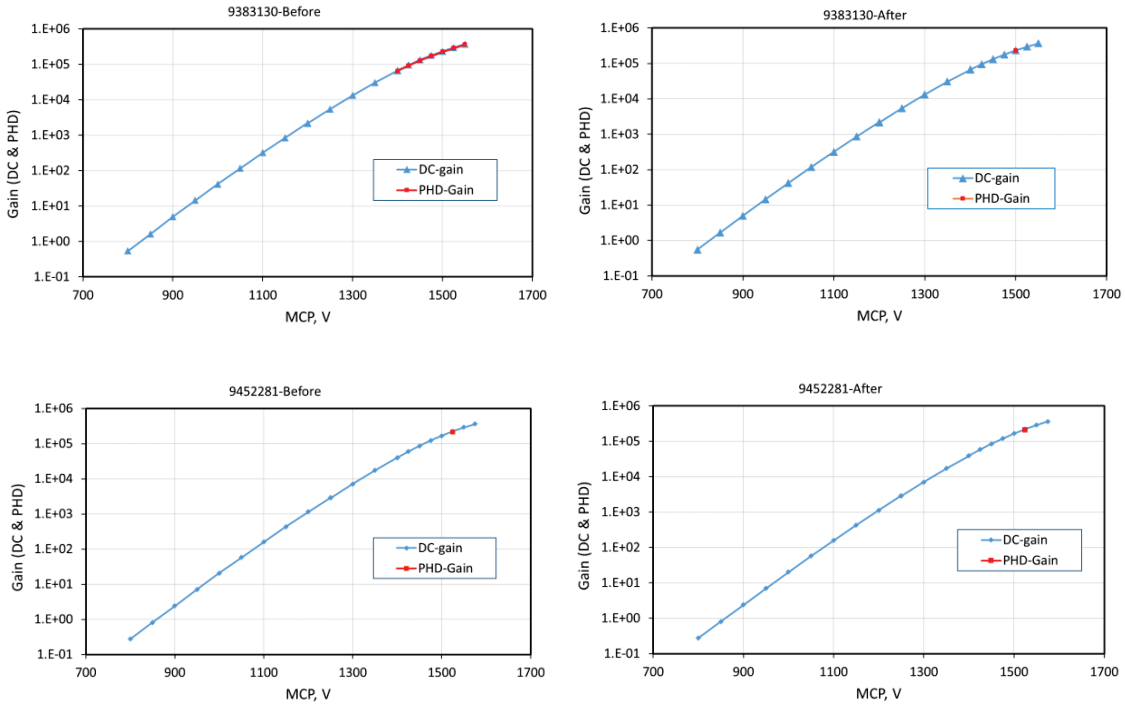

Figure 8. Gain vs MCP voltage for detectors #938130 (top) and #9452281 (bottom) before (left) and after (right) the proton radiation test.

Linearity of the MCP-PMT vs anode current is demonstrated on the Figure 9 with homogenous illumination of full photocathode area (appr. 18mm). Both detectors are high-linearity MCP-PMTs demonstrating extended linearity range. The 0.75 linearity threshold is reached at about 3 μA anode current and 0.5 threshold is at about 5 μA anode current for both MCP-PMT and with no recognizable change after the radiation.

The temporal resolution - defined as the standard deviation of the Gaussian fitting the peak - as well as Pulse Signal FWHM before and after the radiation are very stable.

Small afterpulsing contribution of about 0.06%-0.08% is measured with no large change of afterpulsing after the radiation.

The only recognizable difference was found in dark rates. The dark rate for both detectors were small (below 1 kHz), however small increase was found for both detectors after the radiation test: from 150 cps to 480 cps, and from 215 cps to 540 cps, respectively. It can be explained by small traces of radioactivity of the detector body, even 7-8 weeks after the radiation.

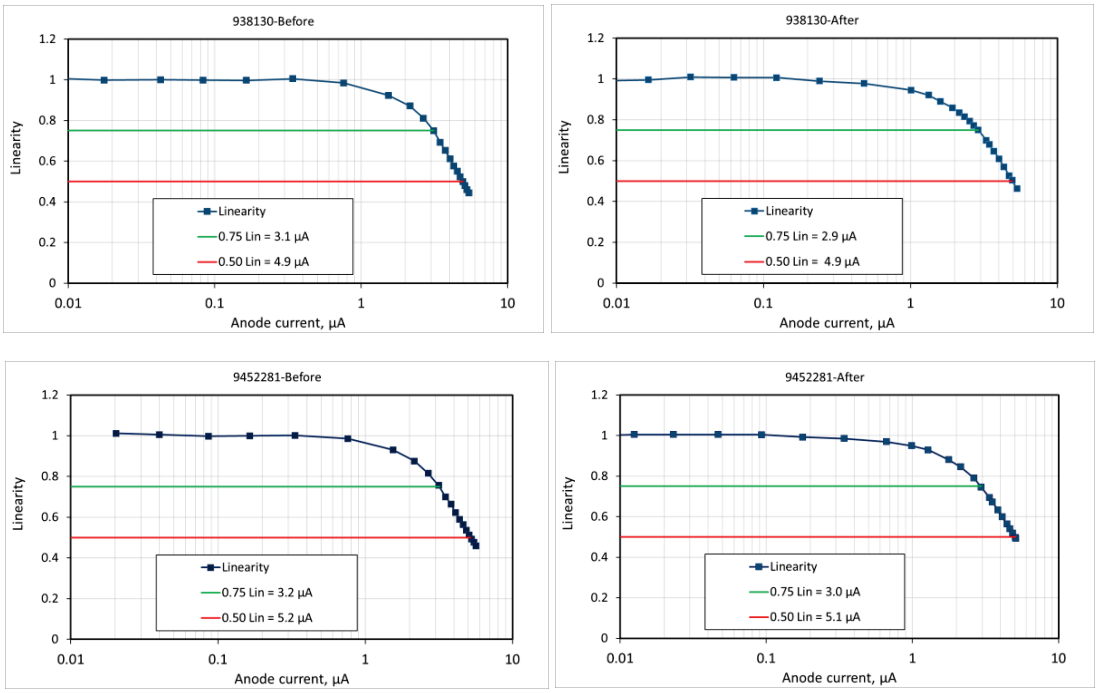

Figure 9. Linearity vs anode current for #938130 (top) and #9452281 (bottom) detectors before (left) and after (right) 60 MeV proton radiation test. The MCP gain is set to about 2.2 10^5 for both detectors.

In flight false pulse occurence

The third radiation phase consisted in a set of four proton energies in the range [30 MeV -185 MeV] and various incident angles (0°, 45°, 60°) to quantify the cross section in order to predict occurrence of false pulses due to protons. The electrons/protons yield was registered for all couples of angle and energies.

Table 3. Calculated cross sections (cm²)

		Cross Sections Device 9383130 (cm²)			Cross Sections Device 1163170 (cm²)		
Energy (MeV)	Angle (°)	Total	Photocathode	MCP	Total	Photocathode	MCP
30	0	3.88	3.82	0.05	5.23	5.01	0.22
	45	3.30	3.19	0.10	4.26	4.11	0.15
	60	2.00	2.00	0.00	2.61	2.61	0.00
60	0	9.68	7.11	2.57	15.43	10.46	4.97
	45	10.14	7.27	2.86	15.23	10.83	4.40
	60	12.71	8.92	3.78	21.27	13.92	7.35
100	0	7.74	5.64	2.10	12.58	8.43	4.14
	45	7.75	5.62	2.13	12.39	8.29	4.10
	60	8.04	5.80	2.24	12.97	8.68	4.29
184	0	6.92	5.51	1.40	10.66	7.93	2.73
	45	6.53	5.13	1.39	10.21	7.49	2.72
	60	6.39	4.98	1.41	9.96	7.24	2.72

The cross section σ was estimated using :

$$\sigma = n_e \frac{S}{\cos(\theta)} \quad (1)$$

Where ne is the quantity of electrons induced by a proton, S is the detector area and θ the angle of incidence.
Table 3 gives the cross-sections for the 2 samples tested.

The obtained cross sections were then used to calculate the mean probability of false event per day depending on the orbit.
The two orbits taken as reference are given in Table 4.

Table 4. Reference cases for false event occurrence

Orbit	Altitude	Type	Inclination	Duration
LEO	400 km	Circular	45°	10 years
LEO	800 km	Circular	98°	10 years

The radiative environment models used for false event forecasting are presented in Table 5.

Table 5. Models used for simulations

Long-term models	Trapped particles	Protons	AP8-min
	Galactic cosmic rays (GCR)	Protons	GCR-ISO solar min
	Solar particles	Protons	ESP, 80%, 6.5 active years

Taking account a Weibull distribution where:

$$\sigma(E) = \sigma_{sat} * \left[1 - \exp\left(-\frac{E-E_{th}}{W}\right)^S\right] \quad (2)$$

with W=35, S=2, E_{th} = 19.9MeV, σ_{sat} = 60cm², for the sample n°9383130, we obtained the false event rate per second for both orbits considered.
The false events per second were calculated using the formula:

$$N = \int_{E=0}^{+\infty} \sigma(E) * Flux(E) * dE \quad (3)$$

Flux and fluences were calculated using OMERE[14]. Other calculations were implemented with Python3.7.
It is interesting to compare the false event rate per second to the photon flux dynamic range ([1 10^5 – 1 10^{12} including max ground echo] photons/s and to the false event rate due to thermal generation in the dark on ground that is about 300 – 500 event/s for our MCP-PMT at room temperature.

Table 6. False event rate (event/s) in the SAA for trapped particles and at the poles for solar particles.

Events/s	400 km, 45°, 10 years	800 km, 98°, 10 years
	0 mm	0 mm
Trapped particles Center of SAA	6 10^4	3.5 10^5
Trapped particles Edge of SAA	10^2	10^2
Solar particles		3 10^3

We observe that, with these worst case assumptions, the false event rate could reach more than 3 10^4 events/s at the very center of the SAA.
Everywhere else, although the particles induced false event rate is larger than the on-ground dark induced false event rate, it remains under the dynamic range threshold of the useful signal.

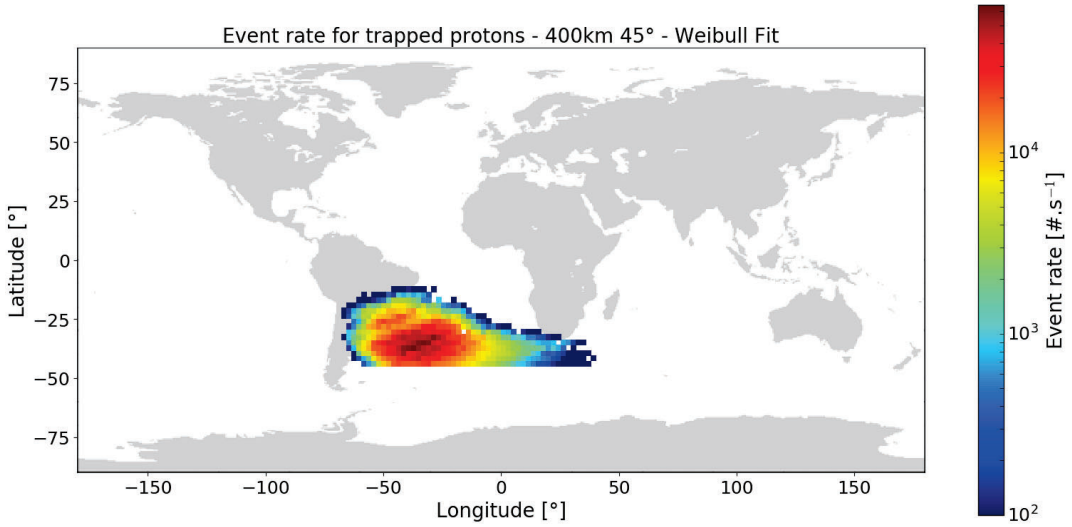

Figure 10. Event rate for trapped protons on a 400 km altitude circular orbit with 45° inclination, with 0mm equivalent aluminum shielding ad Weibull fit.

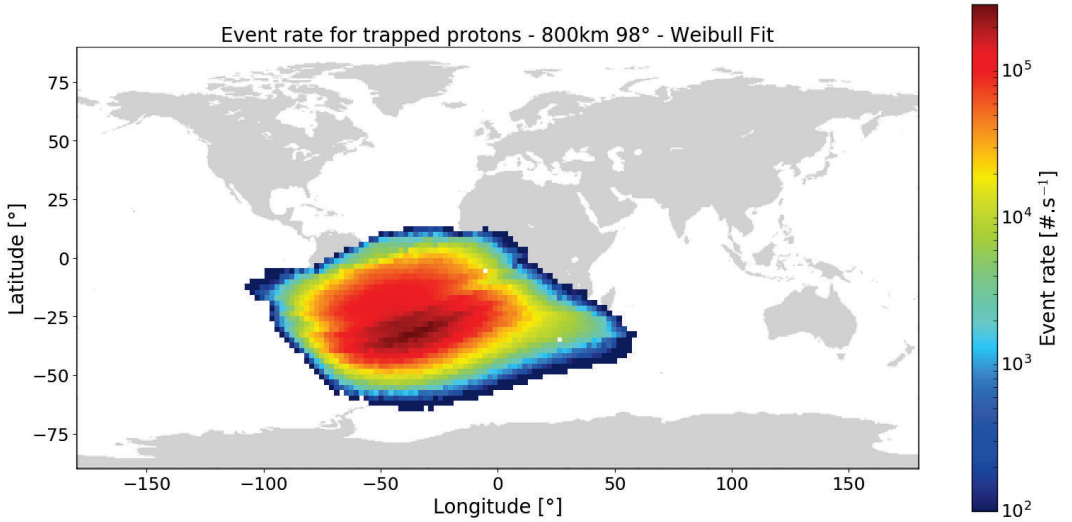

Figure 11. Event rate for trapped protons on a 800 km altitude circular orbit with 98° inclination, with 0mm equivalent aluminum shielding ad Weibull fit.

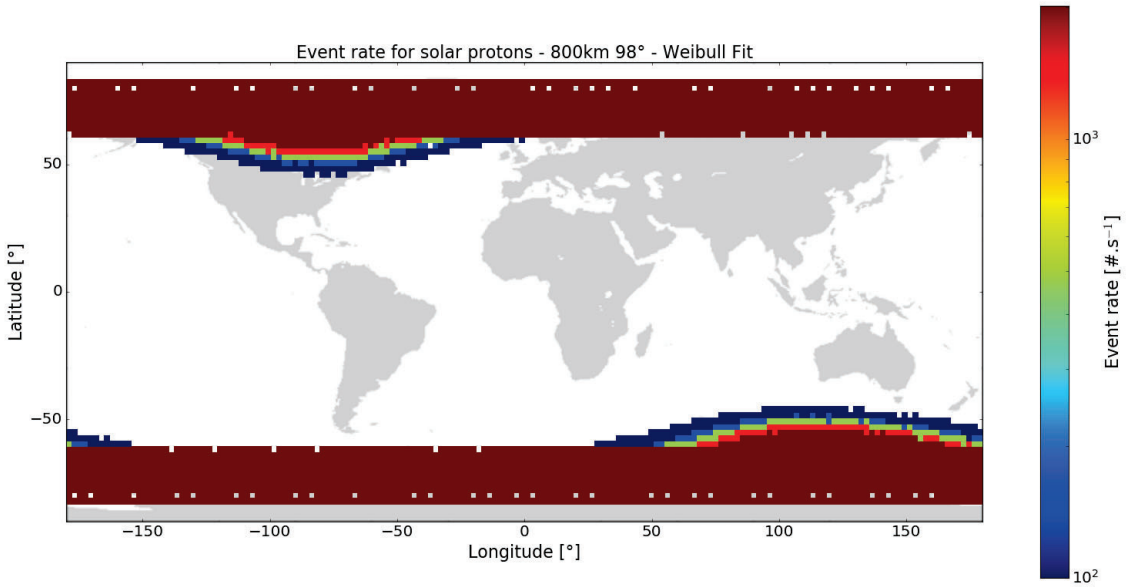

Figure 12. Event rate for solar protons on a 800 km altitude circular orbit with 98° inclination, with 0mm equivalent aluminum shielding ad Weibull fit.

4.4. Electron radiations

No radiation test was performed with electrons as it was estimated that only glass window is impacted up to 2,3 MeV electrons, and 1 MeV electron generates a false event rate 30 electrons at the photocathode for Hi-QE Blue photocathode, with no other damage to the detector.

5. CONCLUSION

A novel design of Hi-QE Blue MCP-PMT has demonstrated promising stability of quantum efficiency up to 20 C of charge generation at the photocathode.
Proton radiation proved no significant changes for LEO missions over more than 10 years equivalent fluences with 4 mm Aluminum shielding.
Results obtained at this step improves TRL of the MCP-PMT technology and consolidates the position of Photonis MCP-PMTs for future space LIDAR missions.

ACKNOWLEDGEMENTS

The authors thank the MESCAL project teams V. Cipolla, R. Schmisser , PJ. Hebert from CNES, M. Schillinger, B. Corselle from Airbus Defence and Space and C. Hostetler from NASA, for inputs provided and fruitful discussions on operating conditions.

REFERENCES

[1] A Beam of LITE: 25 Years of Earth-observing Lidar in Space | NASA https://www.nasa.gov/feature/langley/a-beam-of-lite-25-years-of-earth-observing-lidar-in-space.
[2] Spinhirne,J.D., "Space Borne Cloud and Aerosol Measurements by the Geoscience Laser Altimeter System: Initial Results", XXIII General Assembly of the International Union of Geodesy and Geophysics, Sapporo, 2003.

[3] Winker, D.M. "Status and performance of the CALIOP lidar" Proc. SPIE 5575, Laser Radar Techniques for Atmospheric Sensing; (2004).
[4] Durand,Y., Chinal, E., Endemann,M., Meynart, R., Reitebuch,O., Treichel, R., "ALADIN Airborne Demonstrator: a Doppler Wind Lidar to prepare ESA's ADM-Aeolus Explorer Mission" Proc. of SPIE Vol. 6296, 62961D, (2006).
[5] Weiler,F., Kanitz, T., Wernham,D., Rennie, M., Huber, D., Schillinger, M., Saint-Pe, O., Bell, R., Parrinello,T., Reitebuch,O.," Characterization of dark current signal measurements of the ACCDs used on-board the Aeolus satellite" https://doi.org/10.5194/amt-2020-458.
[6] Jordi Riu, J., Sicard, M., Royo, S., Comerón, A., "Silicon photomultiplier detector for atmospheric lidar applications" OPTICS LETTERS, Vol. 37, No. 7 / 1229-1231 April 1, 2012.
[7] Da Silva, A.M., Maring, H., Seidel, F., Behrenfeld, M., Ferrare, R., Mace, G., "Aerosol, Cloud, Ecosystems (ACE) Final Study Report" NASA/TP–20205007337 September 2020.
[8] Stephan,C., Alpers,M., Millet,B., Ehret,G., Flamant,P., Deniel,C., "MERLIN: a space-based methane monitor," Proc. SPIE 8159, Lidar Remote Sensing for Environmental Monitoring XII, 815908 (13 September 2011); doi: 10.1117/12.896589.
[9] T. Matsumura et al., "Effects of radiation damage caused by proton irradiation on Multi-Pixel Photon Counters (MPPCs)," Nucl. Instrum. Meth., vol. A603, pp. 301–308, 2009.
[10] Chepfer, H., Noel, V., Chiriaco, M.,Wielicki, B., Winker, D., Loeb, N., & Wood, R., "The potential of a multidecade spaceborne lidar record to constrain cloud feedback".Journal of Geophysical Research: Atmospheres,123,5433–5454. https://doi.org/10.1002/2017JD027742 (2018).
[11] High Spectral Resolution LIDAR (HSRL) | NASA Airborne Science Program
[12] Dmitry A. Orlov, René Glazenborg, Raquel Ortega, Emilie Kernen, "From single photon counting to high rate capability with fast timing MCP-PMTs for LIDAR," Proc. SPIE 10978, Advanced Photon Counting Techniques XIII, 109780M (13 May 2019); doi: 10.1117/12.2519061.
[13] D. A. Orlov, R. Glazenborg, R. Ortega, E. Kernen "UV/visible high-sensitivity MCP-PMT single-photon GHz counting detector for long-range lidar instrumentations" CEAS Space Journal. 2019. https://doi.org/10.1007/s12567-019-00260-0.
[14] Peyrard, P. F., Beutier, T., Serres, O., et al. OMERE 2.0 a toolkit for space environment. In IEEE Proceedings of the 7th European Conference on Radiation and its Effects on Components and Systems RADECS. 2003. p. 639-641.